

# Distorting Local Structures to Modulate Ligand Fields in Vanadium Oxide for High-Performance Aqueous Zinc-Ion Batteries

Heng Liu,<sup>#</sup> Long Yang,<sup>#</sup> Ting Shen, Changyuan Li, Te Kang, Huanhuan Niu, Wei-Hsiang Huang, Chun-Chi Chang, Menghao Yang, Guozhong Cao,\* and Chaofeng Liu\*



Cite This: <https://doi.org/10.1021/acsnano.4c18250>



Read Online

ACCESS |

Metrics & More

Article Recommendations

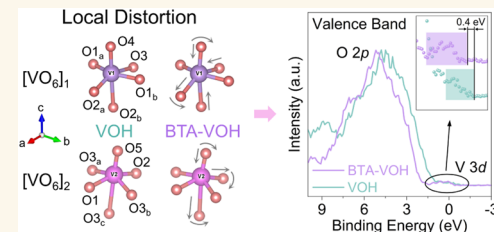
Supporting Information

**ABSTRACT:** Layered hydrate vanadates are promising cathode materials for aqueous zinc-ion batteries (AZIBs). Various intercalants have been preinserted into the interplanar space of hydrate vanadates with significantly enhanced kinetics and stabilized structures. However, such an enhancement is induced by various intercalants, and the relationship between the property enhancement and the type of intercalant still needs to be revealed. In this work, the distortion of octahedra induced by the preintercalation of benzyltrimethylammonium ( $\text{BTA}^+$ ) cations into hydrate vanadium pentoxide ( $\text{V}_2\text{O}_5 \cdot n\text{H}_2\text{O}$ , VOH) and the change in ligand field are studied using synchrotron X-ray pair distribution function (PDF) and X-ray absorption fine structure (XAFS). Variations in the local coordination of vanadium alter the ligand field, decreasing the energy of the lowest unoccupied orbitals ( $e^*$ ), which leads to an increased electrochemical potential. Additionally, the introduced  $\text{BTA}^+$  facilitates fast ion diffusion and stabilizes the layer structure. A cathode with a distorted local structure delivers a specific capacity of 408 mAh/g at 0.5 A/g, with a capacity retention of 95% after 3000 cycles at 8 A/g.

**KEYWORDS:** distorted local structure, ligand field, electrochemical potential, layered hydrate vanadates, aqueous zinc-ion batteries

Recently, aqueous batteries have attracted tremendous attention due to their safety, environmental friendliness, and low cost.<sup>1</sup> Among these, aqueous zinc-ion batteries (AZIBs) stand out because of the high theoretical capacity (820 mAh/g or 5851 mAh/cm<sup>3</sup>) and the relatively low redox potential (−0.76 V versus the standard hydrogen electrode) of the zinc metal anode.<sup>2,3</sup> Various materials have been studied, including manganese oxides,<sup>4–6</sup> Prussian blue, and its analogues,<sup>7–9</sup> polymers,<sup>10,11</sup> and vanadium oxides,<sup>12–15</sup> to screen for suitable candidates with comprehensive properties for the cathode materials of AZIBs. Despite extensive efforts and significant progress, further development of AZIBs is still hindered by slow kinetics, dissolution, and phase transitions of cathode materials.<sup>16</sup>

Vanadium pentoxide ( $\text{V}_2\text{O}_5$ ), a typical vanadium oxide with a layered structure, has a theoretical capacity of 589 mAh/g owing to the variable chemical valence of vanadium from 5+ to 3+.<sup>17,18</sup> However, it suffers from limited practical capacity and poor cycling stability because of its narrow interlayer spacing, significant electrostatic interactions between the  $\text{Zn}^{2+}$  and the [VO] skeleton, and [VO] layers connected by weak van der Waals forces.<sup>19,20</sup> Incorporating water molecules between [VO] layers of  $\text{V}_2\text{O}_5$  could form bilayered hydrated vanadium pentoxide ( $\text{V}_2\text{O}_5 \cdot n\text{H}_2\text{O}$ , denoted as VOH), expanding the



interlayer spacing from 4.4 to 11.9 Å.<sup>17</sup> The electrostatic interaction between  $\text{Zn}^{2+}$  and the V–O framework is reduced due to the shielding effect of lattice water, facilitating ion diffusion and leading to an enhanced capacity (325 mAh/g at 0.5 A/g).<sup>17,21</sup> Preintercalation of guest species, such as inorganic ions ( $\text{Mn}^{2+}$ ,  $\text{Al}^{3+}$ ,  $\text{K}^+$ ,  $\text{Li}^+$ ,  $\text{NH}_4^+$ ,  $\text{Zn}^{2+}$ , etc.),<sup>17,22–30</sup> organic molecules/ions (ethylene glycol,  $\text{N}(\text{CH}_3)_4^+$ ,  $\text{C}_5\text{H}_{14}\text{ON}^+$ ,  $\text{C}_5\text{H}_{13}\text{N}^+$ , etc.),<sup>18,31–35</sup> and polymers (polyaniline, poly(2,3-dihydrothieno-1,4-dioxin), etc.),<sup>36,37</sup> into the interplanar spacing has been demonstrated to be an effective way to improve the electrochemical kinetics and structure stability of VOH. The intercalated inorganic ions exert strong interaction with lattice oxygen ions enhancing structural robustness.<sup>38,39</sup> The preintercalation of organics stabilizes the layered structure via forming hydrogen bonds or electrostatic interactions with [VO] slabs<sup>37</sup> and the conjugated chemical bonds of organics.

Received: December 17, 2024

Revised: February 22, 2025

Accepted: February 24, 2025



ACS Publications

© XXXX American Chemical Society

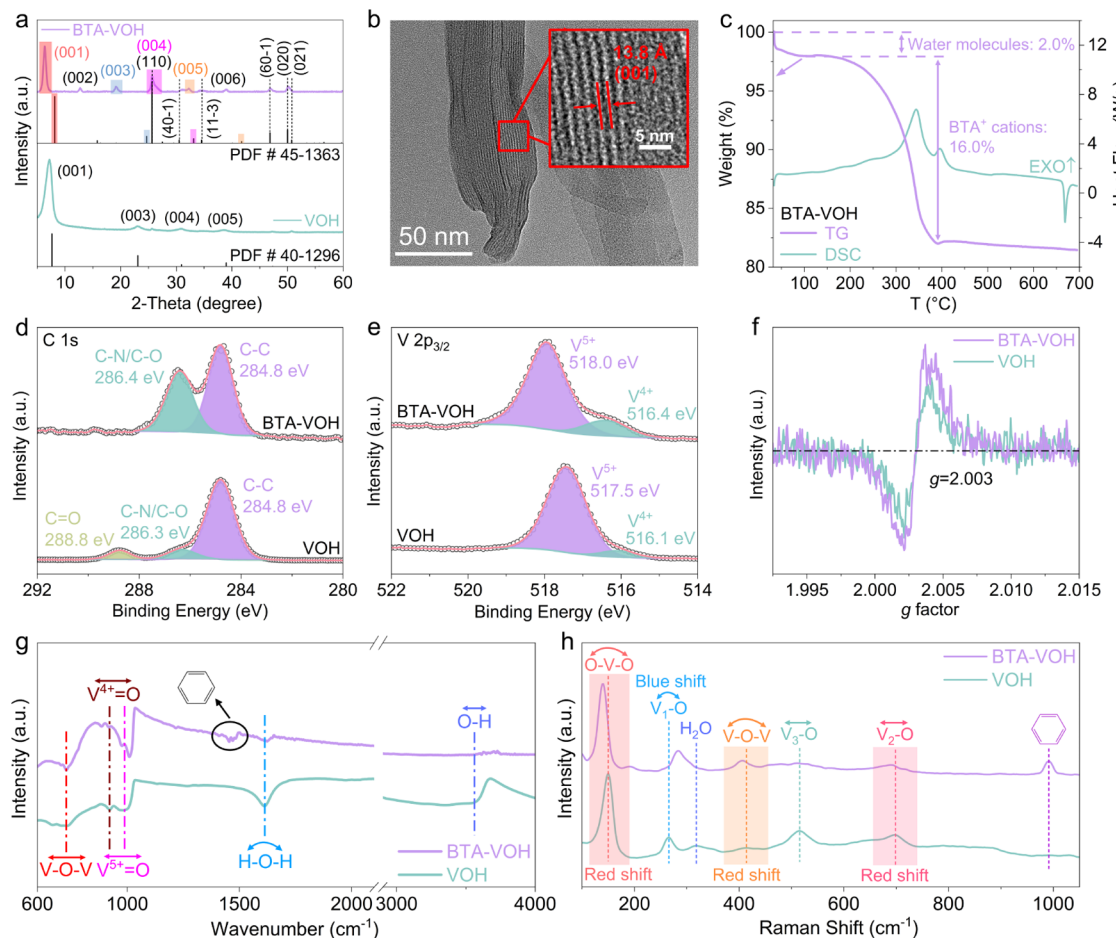


**Figure 1.** Structural, compositional, chemical states, and bonding information of BTA-VOH and VOH. (a) XRD patterns. The lattice spacing of the (001) plane increases from 11.9 to 13.8 Å due to the insertion of  $\text{BTA}^+$ . (b) HRTEM image of BTA-VOH; the spacing of the (001) plane is 13.8 Å. (c) TG/DSC curves of BTA-VOH. The weight loss occurring at 250–400 °C originates from the disintegration of the  $\text{BTA}^+$  cations. (d) High-resolution XPS spectra of C 1s and (e) high-resolution XPS spectra of V 2p<sub>3/2</sub>. (f) EPR spectra. BTA-VOH exhibits a stronger symmetric peak with a *g* value of 2.003, verifying the increased ratio of  $\text{V}^{4+}$  in BTA-VOH. (g) FTIR spectra. The vibration peak of the benzene ring appears in BTA-VOH, demonstrating the introduction of  $\text{BTA}^+$  ions between the layers. (h) Raman spectra. The redshifts of the peaks of the O–V–O bonds, V–O–V bonds, and  $\text{V}_2\text{O}_5$  bonds indicate the elongation of these bonds in BTA-VOH. The blue shift of the V1–O bending vibration peak shows that the V1–O bonds in BTA-VOH are shortened.

can shield the charge of  $\text{Zn}^{2+}$ , alleviating its electrostatic interactions with lattice oxygen.<sup>40</sup> In addition, the flexibility of organics allows them to buffer the lattice strain during charging and discharging.<sup>41,42</sup> Although progress has been made by preintercalation, the influence of intercalants on the local structure of the host lattice and the corresponding changes in the ligand field and the electrical structures of vanadium oxides have received limited attention.

In this study, distorted octahedra in hydrated vanadium pentoxide and the corresponding effects on the electrochemical performance through the preintercalation of an organic cation (benzyltrimethylammonium,  $\text{C}_{10}\text{H}_{16}\text{N}^+$ , BTA $^+$ ) are investigated. It is demonstrated that the introduced BTA $^+$  not only stabilizes the lattice but also induces distortion in the  $[\text{VO}_6]$  octahedra, affecting both the bond length and bond angle. The changes in the coordination structure decrease the energy level of the V 3d orbitals, leading to a lower energy level of the  $t_{2g}^*$  ( $e^*$ ) antibonding orbitals, resulting in a higher electrochemical potential of the modified cathode (BTA-VOH). The organic cation preintercalation expands the interlayer spacing, boosting ion diffusion, and increasing the tetravalent vanadium cations, enhancing electronic conductivity. The BTA-VOH cathode

delivers a specific capacity of 408 mAh/g at 0.5 A/g, with a capacity retention of 95% after 3000 cycles at 8 A/g. The deciphered impacts of the local structure on electrochemical performance provide fundamental guidance for designing next-generation high-performance rechargeable batteries.

## RESULTS AND DISCUSSION

The X-ray diffraction (XRD) patterns of both VOH and BTA-VOH are shown in Figure 1a. VOH is well indexed with textured  $\text{V}_2\text{O}_5 \cdot n\text{H}_2\text{O}$  (PDF# 40-1296) and its highest peak at 7.2° originates from the (001) plane, indicating an interplanar spacing of 12.2 Å. BTA-VOH shows diffraction peaks indexed to the monoclinic  $(\text{Na}, \text{Ca})(\text{V}, \text{Fe})_8\text{O}_{20} \cdot n\text{H}_2\text{O}$  phase (PDF# 45-1363),<sup>43</sup> which is similar to polycrystalline  $\text{V}_2\text{O}_5 \cdot n\text{H}_2\text{O}$ . The (00*l*) peaks of BTA-VOH and  $(\text{Na}, \text{Ca})(\text{V}, \text{Fe})_8\text{O}_{20} \cdot n\text{H}_2\text{O}$  with the same *l* value are marked with the same color, and these peaks of BTA-VOH shift to lower degrees in comparison with  $(\text{Na}, \text{Ca})(\text{V}, \text{Fe})_8\text{O}_{20} \cdot n\text{H}_2\text{O}$  and VOH, indicating the expanded interlayer spacing in BTA-VOH. The lattice plane with a higher *l* value experiences a more significant shift. The positions of the peaks assigned to the (110), (401), (113), (601), (020), and (021) planes remain the same as those in

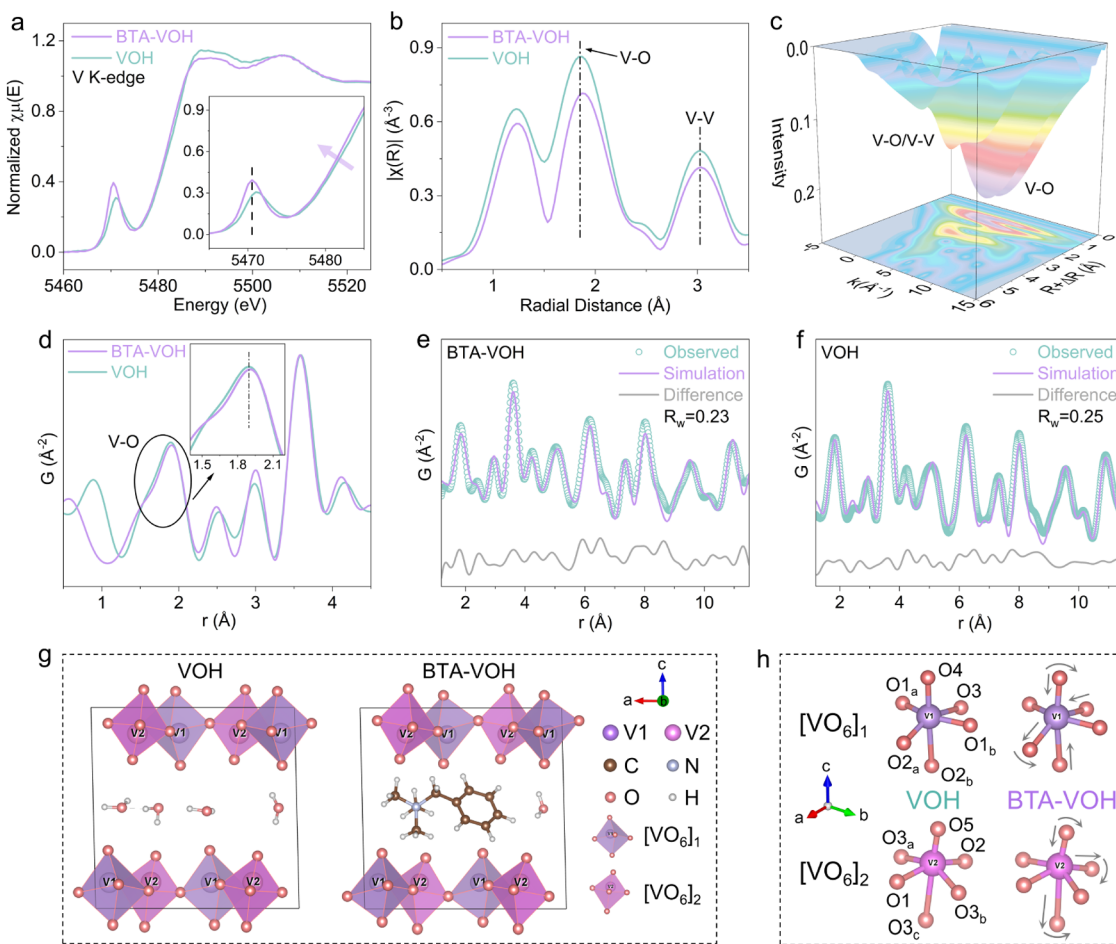


**Figure 2.** Local structure information. (a) V K-edge XAFS spectra. The stronger intensity of the pre-edge peak in BTA-VOH indicates its more highly distorted  $[VO_6]$  polyhedra. (b)  $k^2$ -weighted Fourier transform of the V K-edge EXAFS. The right shift of the peaks is assigned to the V–O interatomic distance, which is along the  $c$ -axis and within the  $ab$  plane, suggesting longer V–O bonds in BTA-VOH. (c) 3D wavelet transforms of BTA-VOH. (d) X-ray pair distribution function (PDF) data of both samples. The peak at  $r \sim 1.9 \text{ \AA}$ , attributed to the V–O interatomic distance, shows a right shift in BTA-VOH, demonstrating the longer V–O bonds in BTA-VOH. PDF refinement results of (e) BTA-VOH and (f) VOH. The experimental PDF data are fit by the  $V_2O_5 \cdot nH_2O$  crystal model over the range of  $1.2 < r < 11.5 \text{ \AA}$ . (g) Crystal structures of both the samples. (h) Schematic illustration of octahedral distortion resolved by PDF local structural refinement. The octahedra in BTA-VOH are distorted compared to those in VOH.

$(\text{Na, Ca})(\text{V, Fe})_8\text{O}_{20} \cdot n\text{H}_2\text{O}$ . The introduced  $\text{BTA}^+$  cations enlarge the interplanar spacing without changing the bilayer structural framework. The interplanar spacing of the (001) plane in BTA-VOH is expanded to  $13.8 \text{ \AA}$ , which is confirmed by the high-resolution transmission electron microscopy (HRTEM) image in Figure 1b. The HRTEM-EDS mapping shown in Figure S1 indicates the homogeneous element distribution of V, O, C, and N in the BTA-VOH nanowires. Thermogravimetric (TG) and differential scanning calorimetry (DSC) analyses of VOH and BTA-VOH were performed, and the results are presented in Figures S2 and 1c, respectively. The total content of water molecules, including adsorbed water (from RT to  $150^\circ\text{C}$ ) and lattice water (from  $150$  to  $350^\circ\text{C}$ ), is 11.5% for VOH. In BTA-VOH, a weight loss of 2.0% occurred accompanied by a weak exothermic peak below  $100^\circ\text{C}$ , resulting from the loss of adsorbed water. The weight loss between  $250$  and  $400^\circ\text{C}$  with the strongest exothermic peak is primarily attributed to the pyrolysis of  $\text{BTA}^+$  cations, indicating that the mass ratio of  $\text{BTA}^+$  cations in BTA-VOH is approximately 16%. The reduced water content in BTA-VOH compared to that of VOH indicates that lattice water escapes in BTA-VOH. The weaker exothermic peak located at

about  $400^\circ\text{C}$  arises from the oxidation of  $\text{V}^{4+}$ <sup>44</sup> resulting in a subtle mass increase. For VOH, this  $\text{V}^{4+}$  oxidation peak is almost absent, indicating a higher content of  $\text{V}^{4+}$  in BTA-VOH than in VOH. Figure 1d shows the high-resolution XPS spectra of C 1s. The characteristic peaks at  $\sim 284.8$  and  $286.4 \text{ eV}$  are assigned to C–C and C–N/C–O, respectively.<sup>45</sup> The signals of carbon in VOH originate from the adventitious carbon contamination.<sup>46</sup> A significant increase in the intensity of the C–N/C–O peak demonstrates the incorporation of organics ( $\text{BTA}^+$ ) in BTA-VOH. The N 1s spectrum of BTA-VOH in Figure S3 also corroborates  $\text{BTA}^+$  incorporation. Figure 1e displays the XPS spectra of V 2p<sub>3/2</sub>. VOH shows two characteristic peaks at  $516.1$  and  $517.5 \text{ eV}$ , corresponding to  $\text{V}^{4+}$  and  $\text{V}^{5+}$ , respectively. For BTA-VOH, these two peaks shift slightly to higher binding energies of  $516.4$  and  $518.0 \text{ eV}$ , respectively, indicating that the incorporation of  $\text{BTA}^+$  cations changes the coordination environment of vanadium and consequently alters the energy level of molecule orbitals, which will be elaborated on in the next section. The ratio of  $\text{V}^{4+}$  in BTA-VOH is 14%, which is higher than that in VOH (8%). The increased proportion of  $\text{V}^{4+}$  is attributed to the intercalation of  $\text{BTA}^+$  cations because of the electroneutrality

**Table 1.** PDF Structural Refinement Results for BTA-VOH and VOH over the Range of  $1.2 < r < 11.5 \text{ \AA}^a$ 

VOH				BTA-VOH			
atom	x	z	$U_{\text{iso}} [\text{\AA}^2]$	atom	x	z	$U_{\text{iso}} [\text{\AA}^2]$
lattice parameter: $a = 11.8637 \text{ \AA}$ , $b = 3.5980 \text{ \AA}$ , $c = 11.7426 \text{ \AA}$ , $\beta = 88.65^\circ$ .				lattice parameter: $a = 11.7556 \text{ \AA}$ , $b = 3.6288 \text{ \AA}$ , $c = 11.7474 \text{ \AA}$ , $\beta = 88.65^\circ$ .			
V (1)	0.9305	0.1280	0.0047	V (1)	0.9292	0.1314	0.0041
V (2)	0.2255	0.1297	0.0047	V (2)	0.2247	0.1306	0.0041
O (1)	0.3838	0.1223	0.0187	O (1)	0.3830	0.1166	0.0284
O (2)	0.0818	0.0767	0.0187	O (2)	0.0847	0.0627	0.0284
O (3)	0.7409	0.0906	0.0187	O (3)	0.7588	0.0949	0.0284
O (4)	0.9346	0.2885	0.0187	O (4)	0.9079	0.2763	0.0284
O (5)	0.1988	0.2576	0.0187	O (5)	0.1913	0.2532	0.0284
O*	0.5939	0.5040	0.0297	O*	0.6098	0.5035	0.0114

<sup>a</sup>Here, x and z are the refinable atomic positions in the fractional coordinates of the V and O sites.  $U_{\text{iso}}$  ( $\text{\AA}^2$ ) is the isotropic atomic displacement parameter (ADP). O\* represents the oxygen of the lattice water.

requirement in BTA-VOH.<sup>17</sup> The EPR signal from both samples in Figure 1f comes from the magnetic moment of unpaired electrons.<sup>47</sup>  $\text{V}^{4+}$  has one unpaired electron, while  $\text{V}^{5+}$  has none. Therefore, BTA-VOH exhibits a stronger symmetric peak with a g value of 2.003, demonstrating a higher ratio of  $\text{V}^{4+}$ . Fourier transform infrared spectroscopy (FTIR) spectra are presented in Figure 1g. The peak located at  $727 \text{ cm}^{-1}$  is assigned to the asymmetric stretching vibration of the V–O–V bonds.<sup>14</sup> The peaks at  $921$  and  $989 \text{ cm}^{-1}$  are attributed to the stretching vibrations of  $\text{V}^{4+}=\text{O}$  and  $\text{V}^{5+}=\text{O}$ ,<sup>21</sup> respectively. The splitting of the  $\text{V}^{4+}=\text{O}$  and  $\text{V}^{5+}=\text{O}$  peaks in BTA-VOH implies changes in the V–O bond length and distortion in the  $[\text{VO}_6]$  octahedra. The peaks at  $1455 \text{ cm}^{-1}$  originate from the ring mode of the benzene ring,<sup>48</sup> which is a chemical species of  $\text{BTA}^+$ . The peaks at  $1612$  and  $3560 \text{ cm}^{-1}$  are related to the bending and stretching vibrations of O–H bonds in lattice water.<sup>21,49,50</sup> The water signal of BTA-VOH is significantly weakened, suggesting that the intercalation of  $\text{BTA}^+$  is accompanied by the expulsion of partial lattice water. The Raman spectra shown in Figure 1h provide structural information for both samples. For VOH, the peaks at  $150$ ,  $414$ , and  $699 \text{ cm}^{-1}$  are assigned to the bending vibrations of O–V–O, V–O–V, and  $\text{V}_2\text{O}$ , respectively.<sup>17,21,51</sup> In BTA-VOH, these three peaks were red-shifted to  $140$ ,  $407$ , and  $691 \text{ cm}^{-1}$ , respectively, indicating the weakening and elongation of these bonds. The peak of  $\text{V}_1\text{O}$  at  $266 \text{ cm}^{-1}$  is ascribed to the bending vibration of the shorter V–O bonds along the c-axis in VOH.<sup>52</sup> The blue shift of this peak in BTA-VOH implies shortening in the corresponding V–O bonds. The undetected water signal ( $318 \text{ cm}^{-1}$ ) in BTA-VOH indicates less lattice water in BTA-VOH. The peak at  $991 \text{ cm}^{-1}$  is assigned to the ring breathing mode of phenyl,<sup>53,54</sup> demonstrating the intercalation of  $\text{BTA}^+$  cations again.

The V K-edge X-ray absorption fine structure (XAFS) spectra are shown in Figure 2a. The intensity of the pre-edge peak is associated with the symmetry and distortion of the  $[\text{VO}_6]$  octahedra.<sup>55</sup> Compared to VOH, BTA-VOH exhibits a higher amplitude of the pre-edge peak, indicating its lower local symmetry and more highly distorted  $[\text{VO}_6]$  octahedra. Compared with VOH, the pre-edge peak and the absorption edge of BTA-VOH both shift to lower energy, indicating the lower valence state of vanadium in BTA-VOH.<sup>56</sup> The  $k^2$ -weighted Fourier transform of the extended X-ray absorption fine structure (EXAFS) unveils the interatomic distance of the coordination shell.<sup>57</sup> As displayed in Figure 2b, the first peak at  $\sim 1.2 \text{ \AA}$ , to a great extent, suffers from background noise and is

unable to accurately provide local structure information. The peak at  $\sim 1.9 \text{ \AA}$  is attributed to the signals of V–O bonds, with the real length ranging from  $1.5$  to  $2.6 \text{ \AA}$ .<sup>58</sup> The peak around  $3.0 \text{ \AA}$  mainly originates from the V–V interatomic distance.<sup>59</sup> For BTA-VOH, the V–O peak shifts slightly to a higher radial distance in comparison with VOH, indicating the increased average V–O bond length in BTA-VOH. This average elongation is attributed to the higher ratio of  $\text{V}^{4+}$  in BTA-VOH, which has a larger ionic radius of  $72 \text{ pm}$  than  $68 \text{ pm}$  for  $\text{V}^{5+}$ .<sup>17</sup> The changed length of V–O bonds results in more highly distorted  $[\text{VO}_6]$  octahedra in BTA-VOH, compared with VOH. In addition, the intensities of the V–O and V–V peaks in BTA-VOH are lower than those in VOH, indicating the decreased coordination numbers of vanadium in BTA-VOH, which is probably attributed to its lower crystallinity. The 3D wavelet transforms (WT) of BTA-VOH from EXAFS spectra are shown in Figure 2c, indicating that the peak at  $3.0 \text{ \AA}$  in Figure 2b originates from V–O and V–V bonds, which have two maxima at about  $4$  and  $7 \text{ \AA}^{-1}$ , respectively.

Synchrotron X-ray atomic pair distribution function (PDF) analyses of both samples are carried out, and the total PDF curves are shown in Figure 2d. Details of the X-ray PDF data processing can be found in Supporting Information (SI). Figure S4 shows the refined partial PDF curves of BTA-VOH and VOH, which demonstrate the contribution of each atomic pair to the total PDF in Figure 2d. The peak at  $\sim 1.9 \text{ \AA}$  represents the average bond length of the V–O bonds. The right shifts of this peak in both the total and partial PDF curves further confirm the longer average V–O bond length in BTA-VOH. The peak located at  $\sim 2.5 \text{ \AA}$  is attributed to the O–O interatomic distance.<sup>63</sup> The left shift of this peak in BTA-VOH indicates a shorter O–O distance. The third peak at  $\sim 3.0 \text{ \AA}$  is mainly contributed to by the combination of V–V and O–O distances. The peak at  $\sim 3.6 \text{ \AA}$  is mostly attributed to the V–V pair distances along the  $a$  and  $b$  axes, forming the motif of the octahedra plane. The position and area of this peak are almost the same in both samples, which indicates that the interlayer structure motif is unchanged. The peaks at radial distances larger than  $4 \text{ \AA}$  originate from the superposition of the V–O, O–O, and V–V pair distances beyond the first coordination shell, which can be analyzed via PDF refinement to obtain more detailed local structure information. The PDF local structural refinements are performed over the range of  $1.2$  to  $11.5 \text{ \AA}$  for the intralayer structure using the  $\text{V}_2\text{O}_5\cdot n\text{H}_2\text{O}$  model, and its crystal structure and lattice parameters are shown in Figure S5. The fitting model shows the monoclinic structure

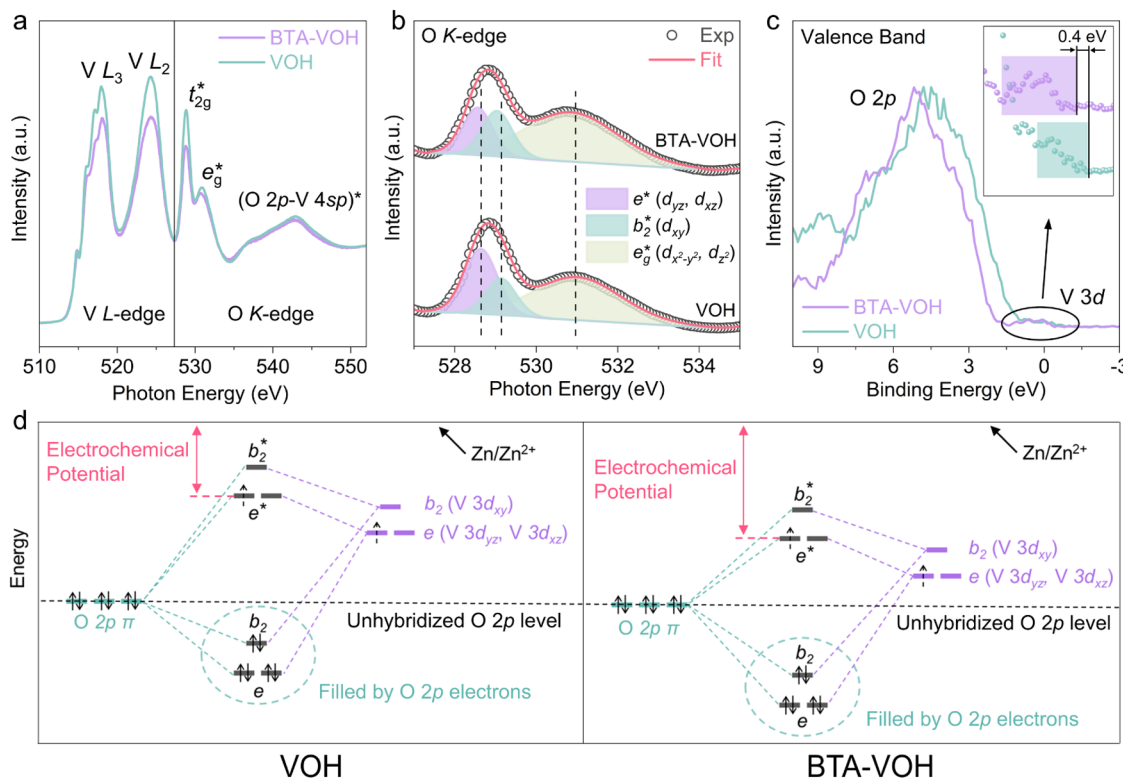


**Figure 3. Orbital energy information.** (a) V L-edge and O K-edge XANES spectra of BTA-VOH and VOH. The lower peak intensity of BTA-VOH is due to its higher V 3d occupancy, validating the lower valence state of vanadium in BTA-VOH. (b) Gaussian fitting of the  $t_{2g}^*$  and  $e_g^*$  peaks for both samples. The  $t_{2g}^*$  antibonding orbital splits into  $e^*$  and  $b_2^*$  orbitals due to the  $C_{4v}$  symmetry of  $[VO_6]$  octahedra in both samples. In BTA-VOH, the  $e^*$ ,  $b_2^*$ , and  $e_g^*$  peaks all shift to lower energies compared with those in VOH. (c) Valence band region of XPS spectra for BTA-VOH and VOH. The O 2p and V 3d bands shift to higher binding energies in BTA-VOH, demonstrating that the introduction of BTA<sup>+</sup> lowers the energy level of electrons from oxygen and vanadium. (d) Schematic illustration of orbital hybridization in BTA-VOH and VOH.

and  $C2/m$  space group, which have the same V–O framework as both samples. Considering that a small amount of lattice water and small organic intercalants contribute to negligible diffraction signals, O atoms are used to represent them for simplifying the fitting process.<sup>64,65</sup> The fitting results and atomic structures are shown in Figure 2e,f and are listed in Table 1. The refined structures of both samples are shown in Figure 2g,h. Two kinds of vanadium atoms with different coordination environments are depicted in diverse colors together with their homologous octahedra ( $[VO_6]_1$  and  $[VO_6]_2$ ). Tables S1 and S2 present refined bond length information on the V–O bonds in BTA-VOH and VOH. Relative to VOH, both elongated and shortened V–O bonds are present in BTA-VOH. As shown in the electron localization function (ELF) sections (Figure S6), the shortening of the V–O bond could be attributed to the intercalated BTA<sup>+</sup> exerting electrostatic interactions on the adjacent oxygen, compressing its electron cloud, which leads to the shortening of the corresponding V–O bonds. In BTA-VOH, for or  $[VO_6]_1$ , the V1–O2<sub>a</sub> bond becomes longer by 0.11 Å, and the V1–O2<sub>b</sub>, V1–O4, and V1–O3 bonds are shortened by 0.15, 0.17, and 0.27 Å, respectively, relative to those in VOH. For  $[VO_6]_2$ , the V2–O2 bond in BTA-VOH is stretched by 0.04 Å. Along the *c*-axis of  $[VO_6]_2$ , the bond length of V2–O5 decreases by 0.06 Å, and the V2–O3<sub>c</sub> bond is elongated by 0.07 Å compared with VOH. The partial bond angle information is presented in Tables S3 and S4, indicating the existence of bond angle deformations after the intercalation of BTA<sup>+</sup>. The bonding

electrons of adjacent bonds repel each other.<sup>66</sup> The variations in the bond length change the repulsion between the bonding electrons in adjacent V–O bonds, leading to a bond angle deformation from a straight to an obtuse angle along the *c*-axis in BTA-VOH. The distortions in bond lengths and angles result in lower symmetric  $[VO_6]$  octahedra in BTA-VOH compared to VOH, which is verified by the higher intensity of the XAFS pre-edge peak in Figure 2a.

Figure 3a shows the V L-edge and O K-edge X-ray absorption near-edge structure (XANES) spectra of both samples. There are two main peaks in the V L-edge (510–527 eV). The L<sub>3</sub> peak is assigned to the dipole-allowed electron transition from V 2p<sub>3/2</sub> to V 3d and the L<sub>2</sub> peak corresponds to the V 2p<sub>1/2</sub> to V 3d transition.<sup>67,68</sup> The decreased peak intensities in BTA-VOH indicate its higher occupancy of V 3d and larger proportion of V<sup>4+</sup>, compared with VOH.<sup>58,69</sup> Based on the crystal field theory, the 5-fold-degenerate V 3d orbitals would be split into two sets of degenerate orbitals ( $e_g$  and  $t_{2g}$ ) in a regular  $[VO_6]$  octahedron.<sup>70</sup> The  $e_g$  orbitals ( $3d_{x^2-y^2}$  and  $3d_{z^2}$ ) are in the higher energy level as they point directly toward the oxygen ions and are subject to greater electrostatic repulsion. The  $t_{2g}$  orbitals ( $3d_{xy}$ ,  $3d_{yz}$ , and  $3d_{xz}$ ) have lower energies because they are directed between oxygen ions, experiencing fewer repulsions. The O K-edge spectra between 527 and 552 eV exhibit three peaks, which correspond to electron transition from O 1s orbital to V 3d ( $t_{2g}$ –O 2p  $\pi$  antibonding orbitals ( $t_{2g}^*$ ), V 3d ( $e_g$ )–O 2p  $\sigma$  antibonding orbitals ( $e_g^*$ ) and V 4sp–O 2p antibonding orbitals,

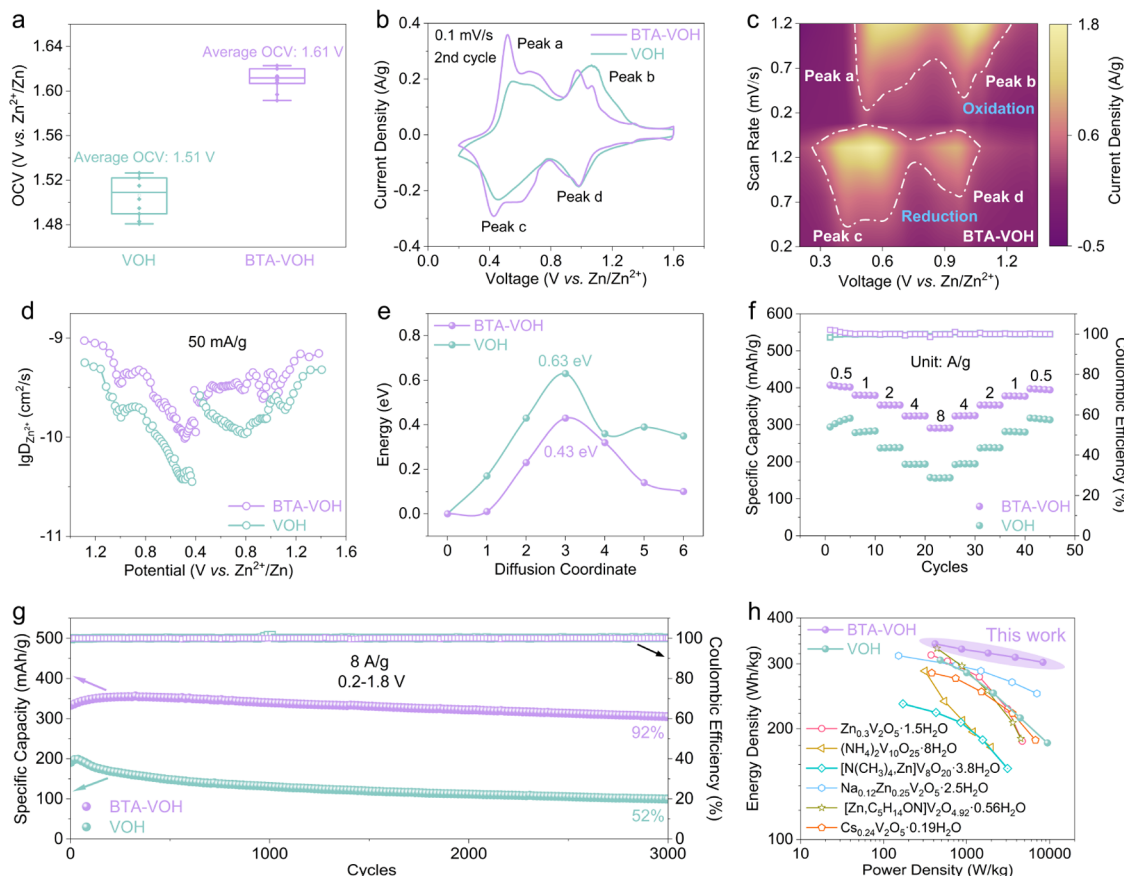


**Figure 4.** Electrochemical properties of BTA-VOH and VOH. (a) Open-circuit voltage statistics from ten batteries. Intercalated  $BTA^+$  ions influence the crystal field of vanadium and lead to a higher open-circuit voltage. (b) CV curves of BTA-VOH and VOH at a scan rate of 0.1 mV/s. For BTA-VOH, the capacity contribution from the  $V^{4+}/V^{3+}$  redox pair around 0.5 V is higher than that of VOH. (c) CV contour of BTA-VOH at various sweep rates from 0.2 to 1.2 mV/s. The change in the redox peaks is intuitively depicted as the sweep rate increases. (d)  $Zn^{2+}$  diffusion coefficients from the GITT tests show that BTA-VOH has higher  $Zn^{2+}$  diffusion coefficients during charging/discharging. (e) Calculated  $Zn^{2+}$  diffusion barriers for pathways in BTA-VOH and VOH. (f) Rate performance at current densities from 0.5 to 8 A/g. (g) Cycling performance at 8 A/g with an expanded voltage range (0.2–1.8 V). BTA<sup>+</sup> intercalation stabilizes the crystal structure to achieve higher capacity retention. (h) Ragone plots. BTA-VOH exhibits competitive energy and power densities in comparison with VOH and reported cathodes at the material level.

respectively.<sup>71</sup> The reduced intensities of these peaks in BTA-VOH are associated with its lower valence state of V and the decreased V–O covalence.<sup>58</sup> The height ratio of  $e_g^*$ / $t_{2g}^*$  peaks in BTA-VOH is higher than that of VOH, which is attributed to the lower valence of vanadium in BTA-VOH. The electronic structures of  $V^{3+}$  are [Ar]3d<sup>0</sup> and [Ar]3d<sup>1</sup> for  $V^{4+}$ . The higher  $V^{4+}$  ratio in BTA-VOH leads to its higher V 3d occupancy and the  $t_{2g}^*$  orbitals are the lowest unoccupied orbitals for both samples. Therefore, the  $t_{2g}^*$  occupancy of BTA-VOH is higher than that of VOH, resulting in a significantly decreased  $t_{2g}^*$  peak intensity.<sup>71</sup> While the  $e^*$  and (O 2p–V 4sp)\* orbitals with higher energy levels than  $t_{2g}^*$  orbitals are much less occupied, they only experience subtle decreases in their intensities. Figure 3b shows the Gaussian fitting results of the  $t_{2g}^*$  and  $e_g^*$  peaks. The  $[VO_6]$  octahedra in both samples present  $C_{4v}$  symmetry, leading to the further splitting of  $t_{2g}^*$  into  $e^*$  and  $b_2^*$  orbitals.<sup>39,69</sup> The electronic structure of  $V^{3+}$  is [Ar]3d<sup>0</sup> and that of  $V^{4+}$  is [Ar]3d<sup>1</sup>. The single 3d electron of  $V^{4+}$  partially occupies the  $e^*$  orbitals, which determines the electrochemical charging/discharging voltage of the first electrons. This occupancy results in a lower absorption intensity of the  $e^*$  peak. As shown in Figure 3b, the  $e^*$ ,  $b_2^*$ , and  $e_g^*$  peaks all shift to lower energies in BTA-VOH relative

to that in VOH. This shift in the  $e^*$  orbitals in BTA-VOH indicates a decrease in the energy level of the lowest unoccupied orbital. Figure 3c shows the valence band region of the XPS spectra. The predominant band at ~5 eV is assigned to the contribution of O 2p electrons.<sup>72,73</sup> The low-intensity band around 0 eV comes from the activation of V 3d electrons, which occupy the  $e^*$  orbitals.<sup>74</sup> For BTA-VOH, both bands shift to lower binding energy compared with VOH, indicating the lower energy levels of O 2p and V 3d ( $e^*$ ). Specifically, the V 3d ( $e^*$ ) band in BTA-VOH shows a left shift of ~0.4 eV, validating the lower energy of the  $e^*$  peak in BTA-VOH, as shown in the O K-edge XANES spectra. Due to the previously discussed averagely elongated V–O bonds in BTA-VOH, the electrostatic repulsion of oxygen ions on the 3d electrons of vanadium is weakened, resulting in the decreased energy of V 3d electrons. In addition, the  $[VO_6]$  octahedra deformation in BTA-VOH, as shown in Figure 2h, leads to the lower symmetric coordination environment, contributing to the more significant splitting of the V 3d orbitals.<sup>75</sup> Specifically, this lower symmetric coordination environment reduces the repulsion on V 3d orbitals within *ab*, *bc*, and *ac* planes ( $3d_{xy}$ ,  $3d_{yz}$ , and  $3d_{zx}$ ) exerted by oxygen ions, causing more significant splitting between  $e_g$  and  $t_{2g}$  orbitals, and bringing  $t_{2g}$  orbitals ( $e$

and  $b_2$  orbitals) to lower energy levels. As illustrated in Figure 3d, owing to the weakened electrostatic repulsion exerted by oxygen ions and the greater 3d splitting in BTA-VOH, the  $t_{2g}$  orbitals, which split into the V 3d<sub>yz</sub> and 3d<sub>xz</sub> orbitals (e) and the 3d<sub>xy</sub> orbital ( $b_2$ ), subsequently shift to lower energy levels than in VOH. Compared with those in VOH, the e-bonding,  $b_2$ -bonding, e\*-antibonding, and  $b_2^*$ -antibonding orbitals in BTA-VOH, formed by the hybridization of O 2p with e and  $b_2$  orbitals, all shift to lower energies.

Figure 4a displays the average open-circuit voltage (OCV) values of both samples. BTA-VOH has an average OCV of 1.61 V, which is higher than that of VOH (1.51 V). The lifted OCV can be attributed to the lower energy of the e\* antibonding orbitals in BTA-VOH. Relative to V 3d electrons, the electrons of O 2p are at a lower energy level; thus, the O 2p electrons preferentially fill the e-bonding and  $b_2$ -bonding orbitals, which have lower energy than the e\* and  $b_2^*$  antibonding orbitals.<sup>70</sup> The single V 3d electron of V<sup>4+</sup> tends to occupy the e\* orbitals, which are the lowest unoccupied orbitals in the V<sup>5+</sup> situation.<sup>58</sup> It is e\* that participates in the electrochemical reactions and relates to the Fermi level of the cathode, determining the electrochemical potential of the BTA-VOH and VOH cathodes. The downshift of the e\* orbitals increases the energy gap with the Fermi level of Zn metal, contributing to the enhanced electrochemical potential of BTA-VOH.<sup>76</sup> Figure 4b is the cyclic voltammetry (CV) curves of both samples collected at 0.1 mV/s. The split redox peaks reflect the splitting of 3d orbitals caused by the [VO<sub>6</sub>] octahedral distortion in the BTA-VOH cathode, which leads to e\* with a distributed energy level that is reflected by the multi peaks and the increased voltage at the lower voltage range in the CV curves.<sup>76,77</sup> As validated by the ex situ XPS spectra of V 2p<sub>3/2</sub> in Figure S7a, when the BTA-VOH cathode is discharged to 0.2 V, V<sup>5+</sup> is reduced to V<sup>4+</sup> and V<sup>3+</sup>. When charged to 1.6 V, V<sup>3+</sup> and V<sup>4+</sup> are reversely oxidized to V<sup>5+</sup>. The proportion of V<sup>4+</sup> in the fully charged state is larger than that in the pristine state, which is attributed to the incomplete deintercalation of Zn<sup>2+</sup> during the charging process of the first cycle, as verified in the ex situ XPS spectra of Zn 2p (Figure S7b). The lattice-trapped Zn<sup>2+</sup> ions during the initial cycle can act as intercalants to stabilize the [VO] layered structure in BTA-VOH.<sup>18</sup> The increased ratio of V<sup>4+</sup> introduced by the lattice-trapped Zn<sup>2+</sup> contributes to the enhanced electrical conductivity.<sup>17</sup> The two major pairs of peaks in the CV curves of both samples indicate a two-step redox reaction. For BTA-VOH, the pair of peaks appearing at 0.98/0.97 V corresponds to the redox pair of V<sup>5+</sup>/V<sup>4+</sup>, and the peaks at 0.52/0.43 V are assigned to the redox pair of V<sup>4+</sup>/V<sup>3+</sup>.<sup>17</sup> VOH exhibits larger voltage differences in the redox pairs (90 mV for V<sup>5+</sup>/V<sup>4+</sup> and 95 mV for V<sup>4+</sup>/V<sup>3+</sup>), indicating the smaller electrochemical polarization in BTA-VOH. The current density of the V<sup>4+</sup>/V<sup>3+</sup> redox peaks in BTA-VOH is significantly larger than that of VOH, indicating a more complete electrochemical reaction in BTA-VOH. Figure S8 shows the CV curves of the initial three cycles at 0.1 mV/s. Compared with VOH, the highly overlapped curves of BTA-VOH indicate high reaction reversibility.<sup>17</sup> Figures 4c and S9 present the CV contours of BTA-VOH and VOH scanned at various scan rates from 0.2 to 1.2 mV/s. The reduction peaks move to lower voltages, and the oxidation peaks move inversely with the increase of the scan rates because of the electrochemical polarization. Additionally, the intensities of the reduction and oxidation peaks increase with the scan rate owing to the improved kinetics by the weakened interaction

between cations.<sup>78</sup> The GITT plots collected at 50 mA/g are shown in Figure 4d. The Zn<sup>2+</sup> diffusion coefficients ( $D_{Zn^{2+}}$ ) of BTA-VOH are  $10^{-10.0}$ – $10^{-9.0}$  cm<sup>2</sup>/s during discharging and  $10^{-9.7}$ – $10^{-9.2}$  cm<sup>2</sup>/s during charging. BTA-VOH has higher  $D_{Zn^{2+}}$  than VOH ( $10^{-10.5}$ – $10^{-9.3}$  cm<sup>2</sup>/s during discharging and  $10^{-10.0}$ – $10^{-9.3}$  cm<sup>2</sup>/s during charging), indicating improved kinetics in BTA-VOH. The preintercalation of BTA<sup>+</sup> cations expands the interlayer spacing and reduces the interactions between Zn<sup>2+</sup> and the [VO] framework,<sup>34</sup> facilitating the diffusion of Zn<sup>2+</sup>. The charge-shielding effect of BTA<sup>+</sup> in BTA-VOH also contributes to the enhanced ion diffusion coefficients as reported in ref 20. The decreased  $D_{Zn^{2+}}$  values during discharging can be attributed to the reciprocal repulsion between the intercalated Zn<sup>2+</sup> ions. The electrostatic interaction between the intercalated Zn<sup>2+</sup> and [VO] layers narrows the interlayer spacing, hindering ion diffusion. As corroborated by the ex situ XRD spectra in Figure S10, during discharging, the (001) peak gradually shifts to a higher angle, indicating shrinkage of the interlayer spacing. When charged to 1.6 V, the interlayer spacing of the (001) plane gradually recovers to its initial state, and the  $D_{Zn^{2+}}$  values increase accordingly. The Zn<sup>2+</sup> diffusion energy barriers in BTA-VOH and VOH are calculated via density functional theory (DFT) to understand the impacts of BTA<sup>+</sup> cations on Zn<sup>2+</sup> migration kinetics. The results are shown in Figure 4e, and the possible migration pathways for Zn<sup>2+</sup> in BTA-VOH and VOH are shown in Figure S11. The Zn<sup>2+</sup> migration barrier in BTA-VOH (~0.43 eV) is much lower than that in VOH (~0.63 eV), indicating faster migration kinetics in BTA-VOH due to the preintercalated BTA<sup>+</sup> cations expanding the interlayer spacing and enlarging the Zn<sup>2+</sup> migration paths. This facilitated ion migration in BTA-VOH, contributing to its higher specific capacity and better rate capability. EIS before and after three cycles of CV testing at 0.1 mV/s is shown in Figure S12. Compared with VOH, BTA-VOH exhibits a lower charge transfer resistance ( $R_{ct}$ ), indicating a higher charge transfer rate in BTA-VOH, which can be attributed to the higher proportion of V<sup>4+</sup> in BTA-VOH. The significant decrease in the  $R_{ct}$  value after the CV test can be attributed to the activation of the electrodes, including the formation of lattice-trapped Zn<sup>2+</sup> enhancing the electrical conductivity and the penetration of electrolyte boosting mass transfer.<sup>17</sup> Figure S13 shows the voltage profiles of BTA-VOH and VOH for the initial three cycles at a rate of 0.5 A/g in the voltage range of 0.2–1.6 V. BTA-VOH delivers a capacity of 402 mAh/g with two charge/discharge plateaus. The plateau in the range of 0.8–1.1 V corresponds to the redox pair V<sup>5+</sup>/V<sup>4+</sup>, while the plateau in the range of 0.65 to 0.35 V is assigned to the V<sup>4+</sup>/V<sup>3+</sup> redox pair, which is significantly weakened in VOH. This indicates a more complete reaction of the V<sup>4+</sup>/V<sup>3+</sup> redox pair in BTA-VOH, which is consistent with the CV results. Compared with VOH (318 mAh/g), BTA-VOH delivers a much higher capacity. The rate capabilities of both samples at various current densities from 0.5 to 8 A/g within the voltage range of 0.2–1.6 V are presented in Figure 4f. At 0.5 A/g, BTA-VOH delivers a capacity of 408 mAh/g, which is much higher than that of VOH (318 mAh/g). As the current densities increase to 1, 2, 4, and 8 A/g, the capacities of BTA-VOH decrease to 380, 354, 326, and 291 mAh/g, respectively, which is superior to those of VOH (283, 239, 194, and 157 mAh/g, respectively). For BTA-VOH, when the current density increases to 8 A/g, the capacity remains 71.3% of the capacity delivered at 0.5 A/g, which is much higher than that

for VOH (49.4%). The faster diffusion of  $Zn^{2+}$  and the enhanced electronic conductivity, as discussed earlier in this paper, contribute to the better rate capability of BTA-VOH. The cycling performances at 8 A/g within 0.2–1.6 V for BTA-VOH and VOH are shown in Figure S14. BTA-VOH delivers an initial capacity of 313 mAh/g and retains 95% of its initial capacity after 3000 cycles, whereas VOH retains 79% of its initial capacity, which is 150 mAh/g. The enhanced cycle stability can be ascribed to the electrostatic interactions between  $BTA^+$  cations and  $[VO]$  slabs stabilizing the layered structure, and the flexibility of  $BTA^+$  buffering the volume strain during zincation and dezincation. Cycling tests of BTA-VOH and VOH with an expanded voltage range (0.2–1.8 V) at 8 A/g are also conducted. The results are shown in Figure 4g. The altered electronic structure, as shown in Figure 3d, leads to a higher average OCV of BTA-VOH (1.61 V) than that of VOH (1.51 V). This lifted electrochemical potential endows the BTA-VOH cathode with higher thermodynamic stability to work steadily in a relatively high voltage range (0.2–1.8 V) with a capacity retention of 92% compared with its initial capacity after 3000 cycles. In addition, the specific capacities of BTA-VOH and VOH both increase when the voltage range is widened. In contrast, VOH suffers much more severe capacity fading when the upper cutoff voltage is raised to 1.8 V. Overall, the merit of BTA-VOH to work stably under an expanded voltage range indicates the increased electrochemical potential caused by the distorted local structure boosts the BTA-VOH cathode to work with a higher voltage, specific capacity, and energy/power density. The cycling test of BTA-VOH at 0.5 A/g is shown in Figure S15. BTA-VOH exhibits a capacity retention of 83% after 100 cycles, indicating its structural stability during deep charging/discharging. Ragone plots of BTA-VOH and VOH at 0.2–1.6 V are displayed in Figure 4h. BTA-VOH exhibits an energy density of 340 Wh/kg at 418 W/kg, which is superior to that of VOH (307 Wh/kg at 482 W/kg) and many reported cathodes.<sup>13,17,18,24,33,38</sup> When charged at 8328 W/kg, BTA-VOH still exhibits an energy density of 303 Wh/kg at the material level. VOH suffers significant energy density fading when charged rapidly, which remains at only 183 Wh/kg at 9407 W/kg. The intercalated  $BTA^+$  cations lead to expanded interplanar spacing and lowered energy levels of the  $e^*$  antibonding orbitals, benefiting  $Zn^{2+}$  diffusion and high electrochemical potential. The electrochemical reaction kinetics and stability are significantly improved in BTA-VOH, resulting in superior electrochemical performance.

## CONCLUSIONS

The distorted local structure in hydrated vanadium pentoxide is induced by the preinserted benzyltrimethylammonium cation ( $BTA^+$ ), which is used as a model to decipher the correlation between the ligand field and electrochemical performance. The distorted  $[VO_6]$  octahedra alter the splitting of the ligand field and reduce the energy level of the reaction electron orbitals ( $e^*$ ), causing an increase in the average OCV in comparison to the pristine hydrated vanadium pentoxide. In addition, the distorted BTA-VOH cathode has an expanded interlayer spacing and a stabilized crystal lattice, enhancing the ion diffusion kinetics and cycling stability. Therefore, the locally structured distorted cathode delivers a specific capacity of 408 mAh/g at a current density of 0.5 A/g and maintains 95% of the initial capacity after 3000 cycles at 8 A/g. This study not only provides a fundamental understanding of the

correlation between the energy level of electron orbitals and the local coordination structure but also paves the way for designing advanced electrode materials on the basis of ligand field theory for next-generation rechargeable batteries.

## METHODS

**Preparation of BTA-VOH and VOH.** All chemicals were used as received without purification. For the preparation of BTA-VOH, 2 mmol of  $V_2O_5$  (99.6%, Sigma-Aldrich) was added to 50 mL of deionized (DI) water and stirred magnetically for 30 min. Then, 2 mL of 30%  $H_2O_2$  (30%, Aladdin) was added and stirred for 30 min to form a black red transparent solution. At the same time, 1 mmol of benzyltrimethylammonium chloride ( $C_{10}H_{16}NCl$ , 99%, Aladdin) was dissolved in 30 mL of DI water to form a colorless transparent solution. The  $C_{10}H_{16}NCl$  solution was then mixed with a transparent  $V_2O_5$  solution, transferred to a 100 mL Teflon-lined stainless steel autoclave, and heated at 120 °C for 6 h. Precipitates were collected by centrifugation and washed with DI water and ethanol 3 times. The precipitates were dried at 70 °C overnight and then further dried at 120 °C for 2 h in a vacuum oven to obtain BTA-VOH powder. VOH was synthesized using the same procedure and conditions without the addition of  $C_{10}H_{16}NCl$ , and the product was dried at –57 °C using a freezing dryer instead of a vacuum oven.

**Material Characterization.** A Rigaku Smartlab X-ray diffractometer with an X-ray generator has a maximum output power of 9 kW X-ray diffraction (XRD) and was utilized for X-ray diffraction (XRD). Stretching and bending information on the chemical bonds was collected using a Fourier transform infrared spectrometer (FTIR, Bruker, VERTEX 70) from 400 to 4500  $\text{cm}^{-1}$ . The Raman spectra were collected using a Thermo Fisher Scientific DXR 2xi Micro-Raman spectrometer. A differential scanning calorimetry and thermogravimetric analysis (DSC/TG, SDT Q600, TA Instruments) were used to investigate the thermal stability of the samples within 40–700 °C in air at a heating rate of 10 °C/min. The morphology and lattice fringes of the samples were characterized using a transmission electron microscope (TEM, JEM-3200FS, JEOL) with an accelerating voltage of 300 kV. X-ray photoelectron spectroscopy was performed using a Thermo Fisher Scientific ESCALAB 250Xi with an Al  $K\alpha$  radiation source that was operated at 10 mA and 15 kV. Electron paramagnetic resonance measurements (Bruker A300) were used to explore the valence state of vanadium. V K-edge X-ray absorption spectra were collected by an easyXAFS300+ benchtop instrument (easyXAFS, LLC) using a Ge (2,1,1) ball-bending crystal analyzer and an Ag anode X-ray tube. Deadtime correction and energy calibration were performed by using a standard V metal foil. Soft-XAS of the V L-edge and O K-edge was performed by the National Synchrotron Radiation Research Center (NSRRC) in Taiwan at the BL20A1 beamline. The experimental PDF data were obtained at BL08W at Super Photon ring-8 GeV (SPring-8) in Japan. It gives the interatomic distance distribution beyond conventional crystallography, i.e., the probability of finding atomic pairs of distance  $r$  apart,<sup>59,80</sup> which can effectively reveal the local atomic distribution in materials. The PDF instrument resolution parameters  $Q_{\text{damp}}$  and  $Q_{\text{broad}}$  were determined as  $Q_{\text{damp}} = 0.0367 \text{ \AA}^{-1}$  and  $Q_{\text{broad}} = 0.0086 \text{ \AA}^{-1}$  by fitting the X-ray PDF from Si collected under the same experimental conditions, which were fixed when refining the sample data sets.<sup>81,82</sup> The minimum and maximum range of data used in the Fourier transform was chosen to be  $Q_{\text{min}} = 0.2230 \text{ \AA}^{-1}$  and  $Q_{\text{max}} = 14.50 \text{ \AA}^{-1}$ .

**Electrochemical Measurements.** For cathode preparation, we uniformly mixed the active material, conductive carbon, and poly(vinylidene fluoride) (PVDF) binder with a weight ratio of 7:2:1 in *N*-methyl-2-pyrrolidone (NMP). The obtained slurry was pasted onto a current collector (titanium foil and stainless steel mesh of 500 mesh for ex situ tests). The obtained electrodes were dried in a vacuum oven at 100 °C for 12 h. The active material loading was about 2–3 mg· $\text{cm}^{-2}$ . Zn metal was used as the anode. A glass fiber filter (Whatman, grade GF/A) was used as the separator, and 80  $\mu\text{L}$  of 3 M zinc trifluoromethanesulfonate (98%,  $Zn(CF_3SO_3)_2$ , Sigma-Aldrich) aqueous solution was dropped into it as the electrolyte. All

electrochemical measurements were based on typical CR2032 coin cells. Electrochemical impedance spectroscopy (EIS) and cyclic voltammetry (CV) were performed on an electrochemical workstation (CHI750E, Chenhua, China). The EIS measurements were carried out at the OCV states from  $10^{-2}$  to  $10^5$  Hz with an amplitude of 0.005 V. The galvanostatic intermittent titration technique (GITT) was applied at a current density of 50 mA/g with a charge/discharge time and interval of 10 min. Galvanostatic charge and discharge tests with different current densities were conducted on a Neware tester (MIHW-200–160CH-B). The working voltage range of the cells was 0.2 to 1.6 V versus  $Zn^{2+}/Zn$ .

**Theoretical Calculations.** DFT calculations were performed based on the Vienna Ab Initio Simulation (VASP) using the projector-augmented wave (PAW) method.<sup>83–86</sup> The Perdew–Burke–Erzerh (PBE) exchange-correlation functional of the generalized gradient approximation (GGA) was adopted. The kinetic energy cutoff of the plane wave was set to 500 eV. We used a density of  $0.04 \times 2\pi \text{ \AA}^{-1}$  k-mesh set to sample the Brillouin zone integration for structural optimization. The energy and force convergence were set at  $2.0 \times 10^{-3}$  eV and  $2.0 \times 10^{-2}$  eV/ $\text{\AA}$ , respectively. The Coulombic interaction (DFT + U)<sup>87</sup> for V 3d electrons was set as a  $U-J$  value of 4.5 eV. The diffusion barriers of the reactions were calculated using the climbing image nudged elastic band (CI-NEB) method, which had been implemented in the VASP transition state tools (VTST).<sup>88</sup>

## ASSOCIATED CONTENT

### Data Availability Statement

Data will be made available on request.

### Supporting Information

The Supporting Information is available free of charge at <https://pubs.acs.org/doi/10.1021/acsnano.4c18250>.

HRTEM-EDS mapping, TG/DSC analyses of VOH, XPS spectra of N 1s, 3D wavelet transform of XAFS spectra, partial PDF curves, crystal structure for PDF fitting, ELF sections, ex situ XPS/XRD spectra, CV curves and contours, calculated  $Zn^{2+}$  migration pathways, EIS spectra, voltage profiles, and cycling performance of both samples at 8 A/g and 0.5 A/g at 0.2–1.6 V ([PDF](#))

## AUTHOR INFORMATION

### Corresponding Authors

**Guozhong Cao** — Department of Materials Science and Engineering, University of Washington, Seattle, Washington 98195, United States; [orcid.org/0000-0001-6539-0490](https://orcid.org/0000-0001-6539-0490); Email: [gzcao@uw.edu](mailto:gzcao@uw.edu)

**Chaofeng Liu** — Interdisciplinary Materials Research Center, School of Materials Science and Engineering, Tongji University, Shanghai 201804, China; [orcid.org/0003-2942-1418](https://orcid.org/0003-2942-1418); Email: [chaofeng@tongji.edu.cn](mailto:chaofeng@tongji.edu.cn)

### Authors

**Heng Liu** — Interdisciplinary Materials Research Center, School of Materials Science and Engineering, Tongji University, Shanghai 201804, China

**Long Yang** — Interdisciplinary Materials Research Center, School of Materials Science and Engineering, Tongji University, Shanghai 201804, China; [orcid.org/0001-8731-0172](https://orcid.org/0001-8731-0172)

**Ting Shen** — Department of Materials Science and Engineering, Clemson University, Clemson, South Carolina 29634, United States

**Changyuan Li** — Interdisciplinary Materials Research Center, School of Materials Science and Engineering, Tongji University, Shanghai 201804, China

**Te Kang** — Interdisciplinary Materials Research Center, School of Materials Science and Engineering, Tongji University, Shanghai 201804, China

**Huanhuan Niu** — Interdisciplinary Materials Research Center, School of Materials Science and Engineering, Tongji University, Shanghai 201804, China

**Wei-Hsiang Huang** — National Synchrotron Radiation Research Center (NSRRC), Hsinchu 300092, Taiwan; [orcid.org/0000-0001-9503-0373](https://orcid.org/0000-0001-9503-0373)

**Chun-Chi Chang** — Graduate Institute of Applied Science and Technology, National Taiwan University of Science and Technology, Taipei 10607, Taiwan

**Menghao Yang** — Interdisciplinary Materials Research Center, School of Materials Science and Engineering, Tongji University, Shanghai 201804, China; [orcid.org/0000-0001-7926-5113](https://orcid.org/0000-0001-7926-5113)

Complete contact information is available at:

<https://pubs.acs.org/10.1021/acsnano.4c18250>

### Author Contributions

#H.L. and L.Y. contributed equally to this work.

### Notes

The authors declare no competing financial interest.

## ACKNOWLEDGMENTS

This work is financially supported by the National Natural Science Foundation of China (52102277, 52302193, and 52472238) and the Fundamental Research Funds for the Central Universities, conducted by Tongji University. C.L. appreciates the XAFS support provided by J.Z. from Quantum Design, China. The authors acknowledge the Experimental Center of Materials Science and Engineering, Tongji University. Soft-XAS Research facilities were provided by the beamline of TLS BL20A1, National Synchrotron Radiation Research Center (NSRRC), Taiwan. The synchrotron radiation PDF experiments were performed at BL08W of SPring-8 with the approval of the Japan Synchrotron Radiation Research Institute (JASRI, Proposal No. 2023A1347).

## REFERENCES

- (1) Jia, X.; Liu, C.; Neale, Z. G.; Yang, J.; Cao, G. Active Materials for Aqueous Zinc Ion Batteries: Synthesis, Crystal Structure, Morphology, and Electrochemistry. *Chem. Rev.* **2020**, *120*, 7795–7866.
- (2) Jin, S.; Shao, Y.; Gao, X.; Chen, P.; Zheng, J.; Hong, S.; Yin, J.; Joo, Y. L.; Archer, L. A. Designing Interphases for Practical Aqueous Zinc Flow Batteries with High Power Density and Highareal Capacity. *Sci. Adv.* **2022**, *8*, No. eabq4456.
- (3) Zeng, Y.; Luan, D.; Lou, X. W. Recent Advances in Electrode Engineering Strategies for Aqueous Zn-Based Batteries. *Chem* **2023**, *9*, 1118–1146.
- (4) Cui, S.; Zhang, D.; Gan, Y. Traditional Electrochemical  $Zn^{2+}$  Intercalation/Extraction Mechanism Revisited: Unveiling Ion-Exchange Mediated Irreversible  $Zn^{2+}$  Intercalation for the  $\delta\text{-MnO}_2$  Cathode in Aqueous Zn Ion Batteries. *Adv. Energy Mater.* **2024**, *14*, No. 2302655.
- (5) Zhang, Y.; Cui, X.; Liu, Y.; Cheng, S.; Cui, P.; Wu, Y.; Sun, Z.; Shao, Z.; Fu, J.; Xie, E. Aqueous  $Zn\text{-MnO}_2$  Battery: Approaching the Energy Storage Limit with Deep  $Zn^{2+}$  Pre-Intercalation and Revealing the Ions Insertion/Extraction Mechanisms. *J. Energy Chem.* **2022**, *67*, 225–232.
- (6) Zeng, Y.; Wang, Y.; Jin, Q.; Pei, Z.; Luan, D.; Zhang, X.; Lou, X. W. Rationally Designed  $Mn_2O_3\text{-ZnMn}_2O_4$  Hollow Heterostructures

- from Metal-Organic Frameworks for Stable Zn-Ion Storage. *Angew. Chem., Int. Ed.* **2021**, *60*, 25793–25798.
- (7) Deng, W.; Li, Z.; Chen, Y.; Shen, N.; Zhang, M.; Yuan, X.; Hu, J.; Zhu, J.; Huang, C.; Li, C.; Li, R. Bidirectional Interface Protection of a Concentrated Electrolyte, Enabling High-Voltage and Long-Life Aqueous Zn Hybrid-Ion Batteries. *ACS Appl. Mater. Interfaces* **2022**, *14*, 35864–35872.
- (8) Liu, J.; Shen, Z.; Lu, C.-Z. Research Progress of Prussian Blue and Its Analogues for Cathodes of Aqueous Zinc Ion Batteries. *J. Mater. Chem. A* **2024**, *12*, 2647–2672.
- (9) Zeng, Y.; Xu, J.; Wang, Y.; Li, S.; Luan, D.; Lou, X. W. Formation of Cumn Prussian Blue Analog Double-Shelled Nanoboxes toward Long-Life Zn-Ion Batteries. *Angew. Chem., Int. Ed.* **2022**, *61*, No. e202212031.
- (10) Li, W.; Xu, H.; Zhang, H.; Wei, F.; Huang, L.; Ke, S.; Fu, J.; Jing, C.; Cheng, J.; Liu, S. Tuning Electron Delocalization of Hydrogen-Bonded Organic Framework Cathode for High-Performance Zinc-Organic Batteries. *Nat. Commun.* **2023**, *14*, No. 5235.
- (11) Wan, F.; Zhang, L.; Wang, X.; Bi, S.; Niu, Z.; Chen, J. An Aqueous Rechargeable Zinc-Organic Battery with Hybrid Mechanism. *Adv. Funct. Mater.* **2018**, *28*, No. 1804975.
- (12) Liang, W.; Che, Y.; Cai, Z.; Tang, R.; Ma, Z.; Zheng, X.; Wu, X.; Li, J.; Jin, H.; Zhu, C.; Chen, T. Surface Decoration Manipulating  $Zn^{2+}/H^+$  Carrier Ratios for Hyperstable Aqueous Zinc Ion Battery Cathode. *Adv. Funct. Mater.* **2023**, *34*, No. 2304798.
- (13) Cai, P.; Wang, K.; He, X.; Li, Q.; Zhang, Z.; Li, M.; Li, H.; Zhou, M.; Wang, W.; Jiang, K. Electric-Field Harmony in  $V_2C/V_2O_5$  Heterointerfaces toward High-Performance Aqueous Zn-Ion Batteries. *Energy Storage Mater.* **2023**, *60*, No. 102835.
- (14) Wang, J.; Wang, J.; Jiang, Y.; Xiong, F.; Tan, S.; Qiao, F.; Chen, J.; An, Q.; Mai, L.  $CaV_6O_{16}\cdot 2.8H_2O$  with  $Ca^{2+}$  Pillar and Water Lubrication as a High-Rate and Long-Life Cathode Material for Ca-Ion Batteries. *Adv. Funct. Mater.* **2022**, *32*, No. 2113030.
- (15) Shi, Y.; Yin, B.; Sun, Y.; Ge, R.; Hu, Y.; Li, J.; Li, H.; Zhang, S.; Ma, T. Mg Ions Intercalated with  $V_3O_7\cdot H_2O$  to Construct Ultrastable Cathode Materials for Aqueous Zinc-Ion Batteries. *Chem. Commun.* **2024**, *60*, 8597–8600.
- (16) Zhang, N.; Chen, X.; Yu, M.; Niu, Z.; Cheng, F.; Chen, J. Materials Chemistry for Rechargeable Zinc-Ion Batteries. *Chem. Soc. Rev.* **2020**, *49*, 4203–4219.
- (17) Liu, C.; Neale, Z.; Zheng, J.; Jia, X.; Huang, J.; Yan, M.; Tian, M.; Wang, M.; Yang, J.; Cao, G. Expanded Hydrated Vanadate for High-Performance Aqueous Zinc-Ion Batteries. *Energy Environ. Sci.* **2019**, *12*, 2273–2285.
- (18) Zong, Q.; Zhuang, Y.; Liu, C.; Kang, Q.; Wu, Y.; Zhang, J.; Wang, J.; Tao, D.; Zhang, Q.; Cao, G. Dual Effects of Metal and Organic Ions Co-Intercalation Boosting the Kinetics and Stability of Hydrated Vanadate Cathodes for Aqueous Zinc-Ion Batteries. *Adv. Energy Mater.* **2023**, *13*, No. 2301480.
- (19) Zhang, F.; Kang, Y.; Zhao, X.; Li, H.; Dong, H.; Wei, W.; Sang, Y.; Liu, H.; Wang, S. Boosting Charge Carrier Transport by Layer-Stacked  $Mn_xV_2O_6/V_2C$  Heterostructures for Wide-Temperature Zinc-Ion Batteries. *Adv. Funct. Mater.* **2024**, *34*, No. 2402071.
- (20) Yan, M.; He, P.; Chen, Y.; Wang, S.; Wei, Q.; Zhao, K.; Xu, X.; An, Q.; Shuang, Y.; Shao, Y.; Mueller, K. T.; Mai, L.; Liu, J.; Yang, J. Water-Lubricated Intercalation in  $V_2O_5\cdot nH_2O$  for High-Capacity and High-Rate Aqueous Rechargeable Zinc Batteries. *Adv. Mater.* **2017**, *30*, No. 1703725.
- (21) Sun, Q.; Cheng, H.; Yuan, Y.; Liu, Y.; Nie, W.; Zhao, K.; Wang, K.; Yao, W.; Lu, X.; Lu, J. Uncovering the Fundamental Role of Interlayer Water in Charge Storage for Bilayered  $V_2O_5\cdot nH_2O$  Xerogel Cathode Materials. *Adv. Energy Mater.* **2022**, *13*, No. 2202515.
- (22) Yang, Y.; Tang, Y.; Fang, G.; Shan, L.; Guo, J.; Zhang, W.; Wang, C.; Wang, L.; Zhou, J.; Liang, S.  $Li^+$  Intercalated  $V_2O_5\cdot nH_2O$  with Enlarged Layer Spacing and Fast Ion Diffusion as an Aqueous Zinc-Ion Battery Cathode. *Energy Environ. Sci.* **2018**, *11*, 3157–3162.
- (23) Kundu, D.; Adams, B. D.; Duffort, V.; Vajargah, S. H.; Nazar, L. F. A High-Capacity and Long-Life Aqueous Rechargeable Zinc Battery Using a Metal Oxide Intercalation Cathode. *Nat. Energy* **2016**, *1*, No. 16119.
- (24) Cao, J.; Zhang, D.; Yue, Y.; Wang, X.; Pakornchote, T.; Bovornratanarak, T.; Zhang, X.; Wu, Z.-S.; Qin, J. Oxygen Defect Enriched  $(NH_4)_2V_{10}O_{25}\cdot 8H_2O$  Nanosheets for Superior Aqueous Zinc-Ion Batteries. *Nano Energy* **2021**, *84*, No. 105876.
- (25) Shan, L.; Yang, Y.; Zhang, W.; Chen, H.; Fang, G.; Zhou, J.; Liang, S. Observation of Combination Displacement/Intercalation Reaction in Aqueous Zinc-Ion Battery. *Energy Storage Mater.* **2019**, *18*, 10–14.
- (26) Zheng, J.; Liu, C.; Tian, M.; Jia, X.; Jahrman, E. P.; Seidler, G. T.; Zhang, S.; Liu, Y.; Zhang, Y.; Meng, C.; Cao, G. Fast and Reversible Zinc Ion Intercalation in Al-Ion Modified Hydrated Vanadate. *Nano Energy* **2020**, *70*, No. 104519.
- (27) Tian, M.; Liu, C.; Zheng, J.; Jia, X.; Jahrman, E. P.; Seidler, G. T.; Long, D.; Atif, M.; Alsalhi, M.; Cao, G. Structural Engineering of Hydrated Vanadium Oxide Cathode by  $K^+$  Incorporation for High-Capacity and Long-Cycling Aqueous Zinc Ion Batteries. *Energy Storage Mater.* **2020**, *29*, 9–16.
- (28) Wang, L.; Huang, K.-W.; Chen, J.; Zheng, J. Ultralong Cycle Stability of Aqueous Zinc-Ion Batteries with Zinc Vanadium Oxide Cathodes. *Sci. Adv.* **2019**, *5*, No. eaax4279.
- (29) Wang, L.; Yan, J.; Hong, Y.; Yu, Z.; Chen, J.; Zheng, J. Ultrahigh-Rate and Ultralong-Life Aqueous Batteries Enabled by Special Pair-Dancing Proton Transfer. *Sci. Adv.* **2023**, *9*, No. eadf4589.
- (30) Chen, D.; Wang, B.; Cui, X.; Yang, H.; Lu, M.; Cai, D.; Han, W. Intercalation-Induced Amorphous Hydrated Vanadium Oxide for Boosted Aqueous  $Zn^{2+}$  Storage. *Chem. Commun.* **2023**, *59*, 1365–1368.
- (31) Wang, M.; Zhang, J.; Zhang, L.; Li, J.; Wang, W.; Yang, Z.; Zhang, L.; Wang, Y.; Chen, J.; Huang, Y.; Mitlin, D.; Li, X. Graphene-Like Vanadium Oxygen Hydrate (VOH) Nanosheets Intercalated and Exfoliated by Polyaniline (PANI) for Aqueous Zinc-Ion Batteries (ZIBs). *ACS Appl. Mater. Interfaces* **2020**, *12*, 31564–31574.
- (32) Ma, X.; Cao, X.; Yao, M.; Shan, L.; Shi, X.; Fang, G.; Pan, A.; Lu, B.; Zhou, J.; Liang, S. Organic–Inorganic Hybrid Cathode with Dual Energy-Storage Mechanism for Ultrahigh-Rate and Ultralong-Life Aqueous Zinc-Ion Batteries. *Adv. Mater.* **2021**, *34*, No. 2105452.
- (33) Zhang, F.; Sun, X.; Du, M.; Zhang, X.; Dong, W.; Sang, Y.; Wang, J.; Li, Y.; Liu, H.; Wang, S. Weaker Interactions in  $Zn^{2+}$  and Organic Ion-Pre-Intercalated Vanadium Oxide toward Highly Reversible Zinc-Ion Batteries. *Energy Environ. Mater.* **2021**, *4*, 620–630.
- (34) Cheng, X.; Xiang, Z.; Yang, C.; Li, Y.; Wang, L.; Zhang, Q. Polar Organic Molecules Inserted in Vanadium Oxide with Enhanced Reaction Kinetics for Promoting Aqueous Zinc-Ion Storage. *Adv. Funct. Mater.* **2023**, *34*, No. 2311412.
- (35) Niu, H.; Liu, H.; Yang, L.; Kang, T.; Shen, T.; Jiang, B.; Huang, W. H.; Chang, C. C.; Pei, Y.; Cao, G.; Liu, C. Impacts of Distorted Local Chemical Coordination on Electrochemical Performance in Hydrated Vanadium Pentoxide. *Nat. Commun.* **2024**, *15*, No. 9421.
- (36) Du, Y.; Wang, X.; Sun, J. Tunable Oxygen Vacancy Concentration in Vanadium Oxide as Mass-Produced Cathode for Aqueous Zinc-Ion Batteries. *Nano Res.* **2021**, *14*, 754–761.
- (37) Li, R.; Xing, F.; Li, T.; Zhang, H.; Yan, J.; Zheng, Q.; Li, X. Intercalated Polyaniline in  $V_2O_5$  as a Unique Vanadium Oxide Bronze Cathode for Highly Stable Aqueous Zinc Ion Battery. *Energy Storage Mater.* **2021**, *38*, 590–598.
- (38) Liu, H.; Hou, X.; Fang, T.; Zhang, Q.; Gong, N.; Peng, W.; Li, Y.; Zhang, F.; Fan, X. Boosting Zinc-Ion Storage in Hydrated Vanadium Oxides via Migration Regulation. *Energy Storage Mater.* **2023**, *55*, 279–288.
- (39) Li, J.; McColl, K.; Lu, X.; Sathasivam, S.; Dong, H.; Kang, L.; Li, Z.; Zhao, S.; Kafizas, A. G.; Wang, R.; Brett, D. J. L.; Shearing, P. R.; Corà, F.; He, G.; Carmalt, C. J.; Parkin, I. P. Multi-Scale Investigations of  $\delta-Ni_{0.25}V_2O_5\cdot nH_2O$  Cathode Materials in Aqueous Zinc-Ion Batteries. *Adv. Energy Mater.* **2020**, *10*, No. 2000058.
- (40) Liu, S.; Zhu, H.; Zhang, B.; Li, G.; Zhu, H.; Ren, Y.; Geng, H.; Yang, Y.; Liu, Q.; Li, C. C. Tuning the Kinetics of Zinc-Ion Insertion/

- Extraction in  $V_2O_5$  by in Situ Polyaniline Intercalation Enables Improved Aqueous Zinc-Ion Storage Performance. *Adv. Mater.* **2020**, *32*, No. 2001113.
- (41) Yao, Z.; Zhang, W.; Ren, X.; Yin, Y.; Zhao, Y.; Ren, Z.; Sun, Y.; Lei, Q.; Wang, J.; Wang, L.; Ji, T.; Huai, P.; Wen, W.; Li, X.; Zhu, D.; Tai, R. A Volume Self-Regulation  $MoS_2$  Superstructure Cathode for Stable and High Mass-Loaded Zn-Ion Storage. *ACS Nano* **2022**, *16*, 12095–12106.
- (42) Chen, S.; Li, K.; Hui, K. S.; Zhang, J. Regulation of Lamellar Structure of Vanadium Oxide Via Polyaniline Intercalation for High-Performance Aqueous Zinc-Ion Battery. *Adv. Funct. Mater.* **2020**, *30*, No. 2003890.
- (43) Evans, H.; Post, J.; Ross, D.; Nelen, J. The Crystal Structure and Crystal Chemistry of Fernandinite and Corvusite. *Can. Mineral.* **1994**, *32*, 339–351.
- (44) Wang, S.; Zhu, K.; Yang, L.; Li, H.; Wang, S.; Tang, S.; Zhang, M.; Abliz, A.; Zhao, F. Synthesis and Study of  $V_2O_5/rGO$  Nanocomposite as a Cathode Material for Aqueous Zinc Ion Battery. *Ionics* **2020**, *26*, 5607–5615.
- (45) Bondarenka, V.; Grebinskij, S.; Kaciulis, S.; Mattogno, G.; Mickevicius, S.; Tvardauskas, H.; Volkov, V.; Zakharova, G. Xps Study of Vanadium–Yttrium Hydrates. *J. Electron Spectrosc. Relat. Phenom.* **2001**, *120*, 131–135.
- (46) Grey, L. H.; Nie, H.-Y.; Biesinger, M. C. Defining the Nature of Adventitious Carbon and Improving Its Merit as a Charge Correction Reference for Xps. *Appl. Surf. Sci.* **2024**, *653*, No. 159319.
- (47) Roessler, M. M.; Salvadori, E. Principles and Applications of EPR Spectroscopy in the Chemical Sciences. *Chem. Soc. Rev.* **2018**, *47*, 2534–2553.
- (48) Smith, B. C. Group Wavenumbers and an Introduction to the Spectroscopy of Benzene Rings. *Spectroscopy* **2016**, *31*, 34–37.
- (49) Hu, L.; Wu, Z.; Lu, C.; Ye, F.; Liu, Q.; Sun, Z. Principles of Interlayer-Spacing Regulation of Layered Vanadium Phosphates for Superior Zinc-Ion Batteries. *Energy Environ. Sci.* **2021**, *14*, 4095–4106.
- (50) Wei, Q.; Liu, J.; Feng, W.; Sheng, J.; Tian, X.; He, L.; An, Q.; Mai, L. Hydrated Vanadium Pentoxide with Superior Sodium Storage Capacity. *J. Mater. Chem. A* **2015**, *3*, 8070–8075.
- (51) Chen, X.; Wang, P.; Feng, Z.; Meng, C.; Zhang, Y. Conductive Polymer Intercalated Vanadium Oxide on Carbon Cloth for Fast Ammonium-Ion Storage in Supercapacitor Applications. *Chem. Eng. J.* **2022**, *445*, No. 136747.
- (52) Huang, H.; Xia, X.; Yun, J.; Huang, C.; Li, D.; Chen, B.; Yang, Z.; Zhang, W. Interfacial Engineering of Hydrated Vanadate to Promote the Fast and Highly Reversible  $H^+/Zn^{2+}$  Co-Insertion Processes for High-Performance Aqueous Rechargeable Batteries. *Energy Storage Mater.* **2022**, *52*, 473–484.
- (53) Salinas-Luna, J.; Mentado-Morales, J. Raman Reference Database for Organic Molecules by Using a Coupled-Optical Fiber Raman Spectrograph. *Phys. Scr.* **2024**, *99*, No. 015504.
- (54) Sakamoto, A.; Tasumi, M. Symmetry of the Benzene Ring and Its Normal Vibrations: The “Breathing” Mode Is Not Always a Normal Vibration of a Benzene Ring. *J. Raman Spectrosc.* **2021**, *52*, 2282–2291.
- (55) Park, S. K.; Nakhanivej, P.; Yeon, J. S.; Shin, K. H.; Dose, W. M.; Volder, M. D.; Lee, J. B.; Kim, H. J.; Park, H. S. Electrochemical and Structural Evolution of Structured  $V_2O_5$  Microspheres During Li-Ion Intercalation. *J. Energy Chem.* **2021**, *55*, 108–113.
- (56) Lv, T.; Zhu, G.; Dong, S.; Kong, Q.; Peng, Y.; Jiang, S.; Zhang, G.; Yang, Z.; Yang, S.; Dong, X.; Pang, H.; Zhang, Y. Co-Intercalation of Dual Charge Carriers in Metal-Ion-Confining Layered Vanadium Oxide Nanobelts for Aqueous Zinc-Ion Batteries. *Angew. Chem., Int. Ed.* **2022**, *62*, No. e202216089.
- (57) Cao, J.; Zhang, D.; Yue, Y.; Yang, X.; Yang, C.; Niu, J.; Zeng, Z.; Kidkhunthod, P.; Wannapaiboon, S.; Zhang, X.; Qin, J.; Lu, J. Unveiling the X-Ray Absorption Chemistry of  $H_{3.78}V_6O_{13}$  Cathode for Aqueous Zinc-Ion Batteries. *Adv. Funct. Mater.* **2023**, *33*, No. 2307270.
- (58) Wang, Y.; Wei, S.; Qi, Z.-H.; Chen, S.; Zhu, K.; Ding, H.; Cao, Y.; Zhou, Q.; Wang, C.; Zhang, P.; Guo, X.; Yang, X.; Wu, X.; Song, L. Intercalant-Induced  $V t_{2g}$  Orbital Occupation in Vanadium Oxide Cathode toward Fast-Charging Aqueous Zinc-Ion Batteries. *Proc. Natl. Acad. Sci. U.S.A.* **2023**, *120*, No. e2217208120.
- (59) Avansi, W.; Maia, L. J. Q.; Ribeiro, C.; Leite, E. R.; Mastelaro, V. R. Local Structure Study of Vanadium Pentoxide 1D-Nanostructures. *J. Nanopart. Res.* **2011**, *13*, 4937–4946.
- (60) Kieffer, J.; Karkoulis, D. Pyfai, a Versatile Library for Azimuthal Regrouping. *J. Phys.: Conf. Ser.* **2013**, *425*, No. 202012.
- (61) Juhás, P.; Davis, T.; Farrow, C. L.; Billinge, S. J. L. Pdfgetx3: A Rapid and Highly Automatable Program for Processing Powder Diffraction Data into Total Scattering Pair Distribution Functions. *J. Appl. Crystallogr.* **2013**, *46*, 560–566.
- (62) Farrow, C. L.; Juhas, P.; Liu, J. W.; Bryndin, D.; Božin, E. S.; Bloch, J.; Proffen, T.; Billinge, S. J. L. Pdfit2 and Pdfgui: Computer Programs for Studying Nanostructure in Crystals. *J. Phys.: Condens. Matter.* **2007**, *19*, No. 335219.
- (63) Petkov, V.; Parvanov, V.; Trikalitis, P.; Malliakas, C.; Vogt, T.; Kanatzidis, M. G. Three Dimensional Structure of Nanocomposites from Atomic Pair Distribution Function Analysis. *J. Am. Chem. Soc.* **2005**, *127*, 8805–8812.
- (64) Trikalitis, P. N.; Petkov, V.; Kanatzidis, M. G. Structure of Redox Intercalated  $(NH_4)_{0.5}V_2O_5 \cdot mH_2O$  Xerogel Using the Pair Distribution Function Technique. *Chem. Mater.* **2003**, *15*, 3337–3342.
- (65) Petkov, V.; Trikalitis, P. N.; Bozin, E. S.; Billinge, S. J. L.; Vogt, T.; Kanatzidis, M. G. Structure of  $V_2O_5 \cdot nH_2O$  Xerogel Solved by the Atomic Pair Distribution Function Technique. *J. Am. Chem. Soc.* **2002**, *124*, 10157–10162.
- (66) Gillespie, R. J. Fifty Years of the VSEPR Model. *Coord. Chem. Rev.* **2008**, *252*, 1315–1327.
- (67) Nordlinder, S.; Augustsson, A.; Schmitt, T.; Guo, J.; Duda, L. C.; Nordgren, J.; Gustafsson, T.; Edström, K. Redox Behavior of Vanadium Oxide Nanotubes as Studied by X-Ray Photoelectron Spectroscopy and Soft X-Ray Absorption Spectroscopy. *Chem. Mater.* **2003**, *15*, 3227–3232.
- (68) Schneider, K.; Nowak, P.; Strączek, T.; Raszka, K.; Figura, A.; Stępiń, J.; Rękas, M.; Kapusta, C. Xas Studies of Vanadium Pentoxide Thin Films. *Nucl. Instrum. Methods Phys. Res., Sect. B* **2023**, *545*, No. 165148.
- (69) Chen, C. L.; Dong, C.; Ho, Y.; Chang, C.; Wei, D.; Chan, T.; Chen, J.; Jang, W.; Hsu, C.; Kumar, K.; Wu, M. Electronic and Atomic Structures of Gasochromic  $V_2O_5$  Films. *EPL (Europhys. Lett.)* **2013**, *101*, No. 17006.
- (70) Assat, G.; Tarascon, J.-M. Fundamental Understanding and Practical Challenges of Anionic Redox Activity in Li-Ion Batteries. *Nat. Energy* **2018**, *3*, 373–386.
- (71) Abbate, M.; Pen, H.; Czyzyk, M. T.; Groot, F. M. F. d.; Fuggle, J. C.; Ma, Y. J.; Chen, C. T.; Sette, F.; Fujimori, A.; Ueda, Y.; Kosuge, K. Soft X-Ray Absorption Spectroscopy of Vanadium. *J. Electron Spectrosc. Redat. Phenom.* **1993**, *62*, 185–195.
- (72) Goodacre, D.; Blum, M.; Buechner, C.; Hoek, H.; Gericke, S. M.; Jovic, V.; Franklin, J. B.; Kittiwatanakul, S.; Söhnle, T.; Bluhm, H.; Smith, K. E. Water Adsorption on Vanadium Oxide Thin Films in Ambient Relative Humidity. *J. Chem. Phys.* **2020**, *152*, No. 044715.
- (73) Sawatzky, G. A.; Post, D. X-Ray Photoelectron and Auger Spectroscopy Study of Some Vanadium Oxides. *Phys. Rev. B* **1979**, *20*, No. 1546.
- (74) Jia, X.; Liu, C.; Wang, Z.; Huang, D.; Cao, G. Weakly Polarized Organic Cation-Modified Hydrated Vanadium Oxides for High-Energy Efficiency Aqueous Zinc-Ion Batteries. *Nano-Micro Lett.* **2024**, *16*, No. 129.
- (75) Hou, Z.; Wang, J.; Dai, N.; Yao, S.; Wang, S.; Ji, Y.; Gao, X.; Zhang, H.; Tang, Z.; Sun, Y.; Li, S.; Liu, Y.; Fu, W.; Nie, K.; Jiang, Y.; Yan, Y. M.; Yang, Z. Eliminating the Mn 3d Orbital Degeneracy to Suppress the Jahn–Teller Distortion for Stable  $MnO_2$  Cathode. *Adv. Energy Mater.* **2023**, *14*, No. 2302477.

- (76) Liu, C.; Neale, Z. G.; Cao, G. Understanding Electrochemical Potentials of Cathode Materials in Rechargeable Batteries. *Mater. Today* **2016**, *19*, 109–123.
- (77) Wang, D.; Jiao, Y.; Shi, W.; Pu, B.; Ning, F.; Yi, J.; Ren, Y.; Yu, J.; Li, Y.; Wang, H.; Li, B.; Li, Y.; Nan, C.; Chen, L.; Shi, S. Fundamentals and Advances of Ligand Field Theory in Understanding Structure-Electrochemical Property Relationship of Intercalation-Type Electrode Materials for Rechargeable Batteries. *Prog. Mater. Sci.* **2023**, *133*, No. 101055.
- (78) Wang, J.; Polleux, J.; Lim, J.; Dunn, B. Pseudocapacitive Contributions to Electrochemical Energy Storage in  $\text{TiO}_2$  (Anatase) Nanoparticles. *J. Phys. Chem. C* **2007**, *111*, 14925–14931.
- (79) Billinge, S. J. L.; Skjaervoe, S. H.; Terban, M. W.; Tao, S.; Yang, L.; Rakita, Y.; Frandsen, B. A. Local Structure Determination Using Total Scattering Data. In *Comprehensive Inorganic Chemistry*, 3rd ed.; Reedijk, J.; Poeppelmeier, K. R., Eds.; Elsevier: Amsterdam, 2023; pp 222–247.
- (80) Underneath the Bragg Peaks, Structural Analysis of Complex Materials. In *Pergamon Materials Series*; Egami, T.; Billinge, S. J. L., Eds.; Elsevier: Amsterdam, 2003; Vol. 7, pp 3–404.
- (81) Lyden, H. A. Measurement of the Conductivity Effective Mass in Semiconductors Using Infrared Reflection. *Phys. Rev.* **1964**, *134*, No. A1106.
- (82) Proffen, T.; Billinge, S. J. L. Pdfff, a Program for Full Profile Structural Refinement of the Atomic Pair Distribution Function. *J. Appl. Crystallogr.* **1999**, *32*, 572–575.
- (83) Kresse, G.; Joubert, D. From Ultrasoft Pseudopotentials to the Projector Augmented-Wave Method. *Phys. Rev. B* **1999**, *59*, No. 1758.
- (84) Blöchl, P. E. Projector Augmented-Wave Method. *Phys. Rev. B* **1994**, *50*, No. 17953.
- (85) Kresse, G.; Hafner, J. Ab Initiomolecular Dynamics for Liquid Metals. *Phys. Rev. B* **1993**, *47*, No. 558.
- (86) Kresse, G.; Furthmüller, J. Efficiency of Ab-Initio Total Energy Calculations for Metals and Semiconductors Using a Plane-Wave Basis Set. *Comput. Mater. Sci.* **1996**, *6*, 15–50.
- (87) Dudarev, S. L.; Botton, G. A.; Savrasov, S. Y.; Humphreys, C. J.; Sutton, A. P. Electron-Energy-Loss Spectra and the Structural Stability of Nickel Oxide: An LSDA+U Study. *Phys. Rev. B* **1998**, *57*, No. 1505.
- (88) Henkelman, G.; Uberuaga, B. P.; Jónsson, H. A Climbing Image Nudged Elastic Band Method for Finding Saddle Points and Minimum Energy Paths. *J. Chem. Phys.* **2000**, *113*, 9901–9904.